

Image is First-order Norm+Linear Autoregressive

Yinpeng Chen¹ Xiyang Dai¹ Dongdong Chen¹ Mengchen Liu¹ Lu Yuan¹
Zicheng Liu¹ Youzuo Lin²

¹ Microsoft ² Los Alamos National Laboratory
{yiche,xidai,dochen,mengcliu,luyuan,zliu}@microsoft.com ylin@lanl.gov

Abstract

This paper reveals that every image can be understood as a first-order norm+linear autoregressive process, referred to as FINOLA, where norm+linear denotes the use of normalization before the linear model. We demonstrate that images of size 256×256 can be reconstructed from a compressed vector using autoregression up to a 16×16 feature map, followed by upsampling and convolution. This discovery sheds light on the underlying partial differential equations (PDEs) governing the latent feature space. Additionally, we investigate the application of FINOLA for self-supervised learning through a simple masked prediction technique. By encoding a single unmasked quadrant block, we can autoregressively predict the surrounding masked region. Remarkably, this pre-trained representation proves effective for image classification and object detection tasks, even in lightweight networks, without requiring fine-tuning. The code will be made publicly available.

1 Introduction

Autoregressive language models in GPT [36, 37, 4] have achieved significant success in the field of natural language processing (NLP). They generate text by predicting the probability distribution of the next word in a sequence, given the previous words in that sequence. The success of autoregressive model (AR) also has been transferred to computer vision, such as iGPT [7] in unsupervised learning,

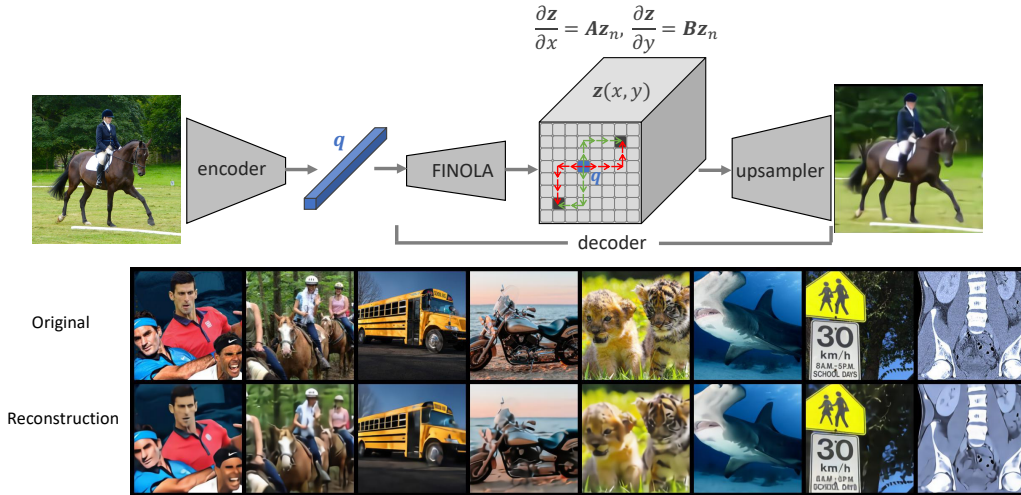


Figure 1: **FINOLA: first-order norm+linear autoregression.** Each image (with size 256×256) is encoded into a single vector q . Then FINOLA is applied on q to generate 16×16 feature map $z(x, y)$ autoregressively which is governed by two partial differential equations (PDEs). Upsampling and convolution are followed to reconstruct the image. Best viewed in color.

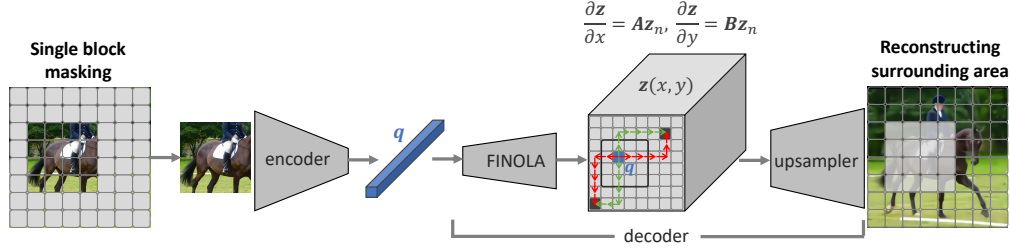


Figure 2: **Masked FINOLA**: a single *unmasked* quadrant block passes through encoder-FINOLA-upsampler network to predict the surrounding *masked* region. Introducing masked prediction into FINOLA trades restoration accuracy for gaining semantic representation.

PixelCNN [43, 40] in image generation and DALL-E [38] in text-to-image generation. These methods share a common characteristic as they apply autoregression over discrete space in a probabilistic manner, i.e. providing a probability distribution over the possible next elements at each step.

In contrast to conventional approaches, this paper models images as a *first-order, norm+linear* autoregressive process over *continuous* space in a *deterministic* manner. Here, norm+linear refers to normalization applied before the linear model. As shown in Figure 1, each 256×256 image can be reconstructed from a single compressed vector q (with C channels) in two steps. Firstly, a 16×16 feature map $z \in \mathbb{R}^{16 \times 16 \times C}$ is generated by placing q at the center (i.e. $z(\frac{16}{2}, \frac{16}{2}) = q$) using first-order norm+linear autoregression (abbreviated as FINOLA) as follows:

$$\begin{aligned} z(x+1, y) &= z(x, y) + \mathbf{A}z_n(x, y) \\ z(x, y+1) &= z(x, y) + \mathbf{B}z_n(x, y) \end{aligned} \quad \text{where} \quad z_n(x, y) = \frac{z(x, y) - \mu_z}{\sigma_z} \quad (1)$$

where the learnable matrices \mathbf{A} and \mathbf{B} , both of size $C \times C$, are shared across all feature positions (x, y) and images. The feature map z is normalized by subtracting the mean μ_z and dividing by the standard deviation σ_z of C channels per position (x, y) , i.e., $\mu_{z(x, y)} = \mathbb{E}_C[z(x, y)]$. Secondly, the image is then reconstructed to its original resolution using a stack of upsampling and 3×3 convolution blocks. Notably, FINOLA operates *deterministically* on a *continuous* latent space, distinguishing it from PixelCNN [43] and DALL-E [38] that compute probability distributions over discrete codebooks [46, 20]. Furthermore, these two steps can be learned jointly end-to-end. The model, trained on the ImageNet-1K [15], achieves reasonably good reconstruction (see examples in Figure 1).

This discovery reveals the latent space can be described by partial differential equations (PDEs) as:

$$\frac{\partial z}{\partial x} = \mathbf{A}z_n, \quad \frac{\partial z}{\partial y} = \mathbf{B}z_n, \quad (2)$$

where z_n denotes the normalized feature map (refer to Equation (1)). In these equations, the coefficient matrices \mathbf{A} and \mathbf{B} capture the relationship between each position and its spatial rate of change. This crucially demonstrates that images possess an *intrinsic mathematical property* within the high-dimensional space. Furthermore, we will demonstrate that this property is a special case of the Laplacian equation, indicating a connection between images and physical systems.

FINOLA is not only beneficial for image compression and reconstruction but also holds potential for self-supervised pre-training. In this study, we propose a novel approach for masked image modeling, utilizing a single unmasked quadrant block and employing FINOLA (or two PDEs) to predict the masked region (see Figure 2). This approach is suitable for lightweight networks (like MobileFormer [14] with 5.8M parameters and 285M FLOPs) and yields a highly capable encoder that can be shared for both image classification and object detection, eliminating the need for fine-tuning.

After comparing FINOLA and masked FINOLA, we discovered that introducing masked prediction sacrifices restoration accuracy in favor of gaining semantic representation, leading to notable improvements in both linear probing and fine-tuning on ImageNet classification. Additionally, masked FINOLA demonstrates a significant increase in Gaussian curvature on the surfaces of critical features, indicating a greater curvature of the latent space for capturing semantics.

It is important to note that our work does not strive for state-of-the-art performance. Instead, our objective is to highlight the significance of the first-order norm+linear autoregressive (FINOLA) property, represented as partial differential equations (PDEs), in images. This property is useful for various tasks like image compression, reconstruction, and self-supervised representation learning.

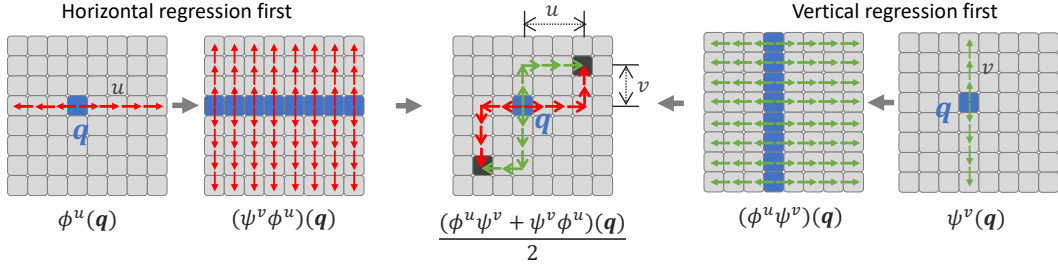


Figure 3: **Parallel implementation of FINOLA:** Horizontal and vertical regressions are separated. In the *left* approach, horizontal regression is performed first, enabling parallel execution of subsequent vertical regression. Similarly, in the *right* approach, vertical regression precedes horizontal regression, enabling parallel implementation of the latter. These options are averaged, corresponding to averaging the two autoregression paths from the center where q is located. Best viewed in color.

2 First-Order Norm+Linear Autoregression

This section provides a detailed explanation of utilizing the first-order norm+linear autoregression, referred to as FINOLA, to reconstruct an image of size 256×256 from a single compressed vector. FINOLA is a simplified autoregression process, characterized by two key constraints: "first-order" and "norm+linear". Despite these simplifications, it is capable of reconstructing high-quality images. Furthermore, our approach reveals that the latent space is governed by two partial differential equations (PDEs), offering insights into the underlying mathematical principles. This novel understanding provides a fresh perspective on images originating from a high-dimensional latent space.

Encoder-FINOLA-upsampler architecture: Let us first introduce the network architecture used to study FINOLA. It consists of three components (see Figure 1): (a) an *encoder* that compresses a 256×256 image into a single C -dimensional vector $q \in \mathbb{R}^C$, (b) *FINOLA* block, which uses first-order norm+linear autoregression to generate a 16×16 feature map $z \in \mathbb{R}^{C \times 16 \times 16}$ with q placed at the center, and (c) an *upsampler* that restores the image to its original resolution of 256×256 . We use Mobile-Former [14] as the encoder and follow the approach of VQGAN [20] to stack upsampling and convolution blocks to construct the upsampler. The whole network is trained end-to-end, by using mean square error over image pixels as loss. Next, we describe FINOLA in detail.

FINOLA: FINOLA autoregressively generates a 16×16 feature map from a single vector q . It employs two $C \times C$ matrices, denoted as A and B , to perform autoregression along the x and y axes separately as shown in Equation (1). It has three characteristics: (a) *first-order* i.e. using only the most recent outcome to predict future values, (b) *norm+linear*, i.e. applying linear models after normalization, and (c) *deterministic in the continuous space* different from PixelCNN [43] and DALL-E [38] that compute probability distributions over discrete codebooks [46, 20]

Despite being a first-order model, FINOLA has the ability to directly autoregress for any position by iteratively applying normalization and linear models as follows:

$$\begin{aligned} z(x+u, y) &= \phi^u(z(x, y)) \\ z(x, y+v) &= \psi^v(z(x, y)) \end{aligned} \quad \text{where } \phi(z) = z + \frac{A(z - \mu_z)}{\sigma_z}, \quad \psi(z) = z + \frac{B(z - \mu_z)}{\sigma_z}. \quad (3)$$

Diagonal prediction from $z(x, y)$ to $z(x+u, y+v)$ is achieved straightforwardly by combining the equations as $(\phi^u \psi^v + \psi^v \phi^u)/2$. To handle autoregression towards the left and down, which involves solving a complex inverse problem, we introduce two additional learnable matrices, A_- and B_- . Specifically, we express $z(x-1, y)$ as $z(x, y) + A_- z_n(x, y)$. Notably, the matrices A and B are shared across all feature positions and images, capturing the intrinsic spatial structures in images.

Parallel implementation: Autoregression can be computationally intensive due to its sequential nature. However, FINOLA leverages the separation of the x and y axes to enable parallel implementation, which significantly speeds up the process. As depicted in Figure 3, by performing horizontal regression first, the subsequent vertical regression can be executed in parallel. Similarly, switching the order to perform vertical regression first enables parallel implementation of horizontal regression. In practice, these two options are combined by averaging the results, where each element represents the average of the two autoregression paths from the center, where q is located.

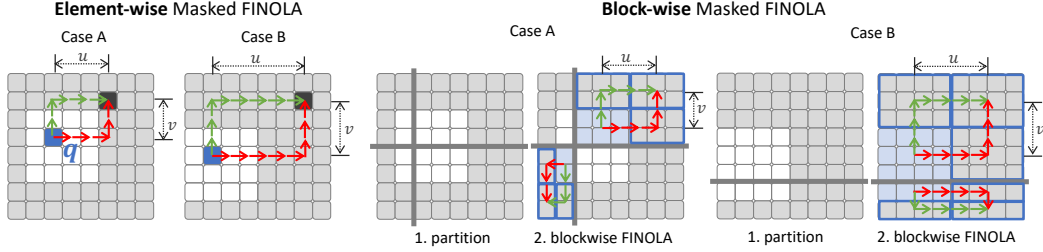


Figure 4: **Masked FINOLA** comprises two variants: element-wise and block-wise approaches. In the element-wise approach (*left*), autoregression is performed similarly to vanilla FINOLA, with the compressed vector q observing only the unmasked block instead of the entire image. In the block-wise approach (*right*), the unmasked block is not compressed but partitioned into sub-blocks, and block-wise autoregression is applied. It is important to note that the block-wise autoregression also follows Equation (3), where u and v represent block offsets. Best viewed in color.

Governing Partial Differential Equations (PDEs): FINOLA sheds light on the underlying partial differential equations (PDEs) governing the latent feature space. By simply extending x and y in Equation 1 from discrete grid indices to continuous coordinates, we can straightforwardly derive the two PDEs $\frac{\partial z}{\partial x} = \mathbf{A}z_n$ and $\frac{\partial z}{\partial y} = \mathbf{B}z_n$ in Equation 2. This indicates that each image corresponds to a continuous surface in the high-dimensional latent space, satisfying these two PDEs. It is important to note that these PDEs are non-linear due to the normalization. Moreover, these two PDEs correspond to a special case of an *anisotropic Laplacian*, which can be expressed as:

$$\frac{\partial^2 z}{\partial x^2} - (\mathbf{A}\mathbf{B}^{-1})^2 \frac{\partial^2 z}{\partial y^2} = 0. \quad (4)$$

Below, we present a concise proof. Please refer to Appendix A for a detailed explanation.

$$\frac{\partial^2 z}{\partial x^2} = \mathbf{A} \frac{\partial z_n}{\partial x} = \mathbf{A}\mathbf{B}^{-1} \frac{\partial^2 z}{\partial x \partial y} \stackrel{*}{=} \mathbf{A}\mathbf{B}^{-1} \frac{\partial^2 z}{\partial y \partial x} = \mathbf{A}\mathbf{B}^{-1} \mathbf{A} \frac{\partial z_n}{\partial y} = \mathbf{A}\mathbf{B}^{-1} \mathbf{A}\mathbf{B}^{-1} \frac{\partial^2 z}{\partial y^2}, \quad (5)$$

where $\stackrel{*}{=}$ denotes the use of Clairaut’s theorem, i.e. $\frac{\partial^2 z}{\partial x \partial y} = \frac{\partial^2 z}{\partial y \partial x}$ when $z(x, y)$ possesses continuous second partial derivatives. This mathematical property connects images to physical systems.

3 Masked FINOLA

In this section, we demonstrate how to use FINOLA in self-supervised learning via a simple masked prediction task. We name it Masked FINOLA to distinguish from the vanilla FINOLA. It is important to notify that masked FINOLA trades reconstruction accuracy for gaining semantic representation.

Simple block masking: We introduce a simple masked prediction design that involves using a single unmasked image block (see Figure 4) to predict the surrounding masked region. Specifically, we crop out the unmasked block and pass it through the encoder, leveraging the power of FINOLA to generate a full-size feature map. Finally, the upsampler is applied to recover the entire image. Unlike vanilla FINOLA, the reconstruction loss is computed only from the masked region. Please note that the unmasked block floats around the image randomly.

Masked FINOLA variants: Masked FINOLA consists of two variants: the element-wise approach (Masked-FINOLA-E) and the block-wise approach (Masked-FINOLA-B), as illustrated in Figure 4.

The element-wise variant (Masked-FINOLA-E) operates similarly to vanilla FINOLA, with the compressed vector q only observing the unmasked block instead of the entire image. To accommodate the longer training required in masked FINOLA (e.g., 1600 epochs), we replace the upsampler with a simple linear layer that transforms a C -channel token into a $16 \times 16 \times 3$ image patch.

The block-wise variant (Masked-FINOLA-B) operates differently, utilizing the features of the unmasked block directly, without compressing it. It requires the unmasked block to have a quadrant size and performs block-wise autoregression in two steps: (a) partitioning the image such that each partition contains an unmasked corner quadrant (see Figure 4), and (b) conducting block-wise autoregression for each partition from the unmasked quadrant to the other three masked quadrants. The

Table 1: **FINOLA vs. masked FINOLA** on ImageNet-1K. Masked FINOLA variants sacrifice restoration accuracy in exchange for improved semantic representation. Block-wise masked FINOLA outperforms the element-wise variant, achieving higher accuracy in linear probing (*lin*), probing with a single transformer block (*tran-1*), and fine-tuning (*tran-1-ft*).

model	encoder output	autoregression	upsampler	recon(PSNR)	lin	tran-1	tran-1-ft
FINOLA	1×1	element-wise	up+conv	25.8	17.9	46.8	81.9
Masked FINOLA-E	1×1	element-wise	linear	16.7	54.1	67.8	82.2
Masked FINOLA-B	8×8	block-wise	trans+linear	17.3	66.4	78.7	82.5

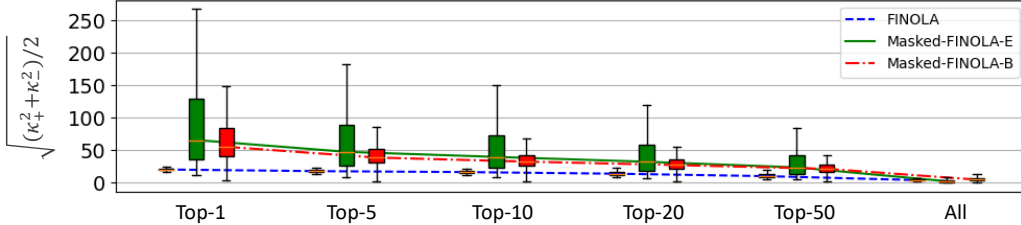


Figure 5: **FINOLA vs. masked FINOLA on Gaussian curvature of critical features:** Evaluation on 50k IN-1K validation images involves analyzing features represented as 16×16 surfaces in 3D space (x, y, z_k) . Gaussian curvature is computed for all channels at each grid element. Channels within each image are sorted based on the root square mean of peak positive (κ_+) and negative curvatures (κ_-), and the distribution is plotted for the top-K features. Masked FINOLA exhibits significantly larger curvature on critical features than vanilla FINOLA, indicating the effectiveness of masked prediction in curving the latent space to capture semantics. Best viewed in color.

block-wise approach ensures consistent processing of elements within the unmasked quadrant for generating predictions in the masked quadrants. Block-wise prediction is performed *autoregressively* using Equation 3 with block offsets u and v . In Masked-FINOLA-B, transformer blocks are incorporated into the upsampler for spatial communication, while Masked-FINOLA-E achieves this by compressing features into q followed by element-wise autoregression.

FINOLA vs. masked FINOLA: Table 1 compares vanilla FINOLA with two masked FINOLA variants, evaluating their architectural differences and performance in image reconstruction and classification. Introducing masking sacrifices restoration accuracy in exchange for improved semantic representation. Among masked FINOLA variants, the block-wise approach outperforms the element-wise counterpart, indicating the difficulty of masked prediction after compression. Figure 5 provides a geometric comparison. Masked FINOLA exhibits a significant increase in Gaussian curvature on the surfaces of critical features, suggesting a greater curvature in the latent space for capturing semantics.

Relation to MAE [25]: Masked FINOLA has a similar architecture to MAE, with differences in *masking* and *prediction*. Firstly, Masked FINOLA utilizes a *regular masking design* by grouping all unmasked patches into a single block, in contrast to MAE’s random unmasked patches. This design choice suits efficient CNN-based networks without unnecessary complexities. Secondly, Masked FINOLA employs a first-order norm+linear autoregression approach to predict the masked region, mathematically represented by two partial differential equations (PDEs).

4 Image Reconstruction Experiments

We evaluate FINOLA for image reconstruction on ImageNet-1K [15]. Please refer to Appendix B and C for model and training details. Below, we report major ablations and findings.

Is normalization necessary in FINOLA? In an attempt to explore the possibility of removing normalization in FINOLA, we investigate the applicability of a trick used in batch normalization. This trick involves utilizing pre-computed moving averages to normalize the input during inference. However, our experiments reveal that this approach does not yield the desired results. Although the training phase exhibits low error rates or high peak signal-to-noise ratios (PSNR=25.1), the inference phase shows a significant increase in error or decrease in PSNR (16.3). Consequently, these findings indicate that normalization is necessary in FINOLA.

Table 2: **Image reconstruction ablation experiments** on ImageNet-1K. We report PSNR on the validate set. The reconstruction quality correlates to (a) the number of channels in the latent space and (b) complexity of encoder. Default settings are marked by \dagger .

#Channels	4096	3072 \dagger	2048	1024	512	256	128	64	Encoder	67.6M	43.5M	25.0M \dagger	12.0M	5.0M
PSNR	25.9	25.8	25.1	23.7	22.2	20.8	19.4	18.2	PSNR	26.1	26.0	25.8	25.1	24.4

(a) Number of channels in latent space.

(b) Model size of encoders.



Figure 6: **Image reconstructon examples.** The leftmost column shows the original images. The number of channels in the latent space, decreasing from 4096 to 64 from the left to right, controls the reconstruction quality. Best viewed in color.

Main architecture hyper-parameters: We investigate two crucial architecture parameters: (a) the number of latent channels, and (b) the encoder model size. By default, Mobile-Former [14] with 25M parameters is used as encoder and the dimension of latent space is set to 3072.

The number of channels in the latent space is crucial. Table 2-(a) presents the PSNR values for various latent space dimensions, while Figure 6 showcases the corresponding reconstructed examples. The image quality is noticeably poor when using only 64 channels, resulting in significant loss of details. However, as the number of channels increases, more details are successfully recovered. Using more than 3072 channels yields reasonably good image quality, achieving a PSNR of 25.8.

The model size of encoder is less critical but also related. As shown in Table 2-(b), the larger model has better image quality. But the gap is not significant. When increasing model size by 13 times from 5.0M to 67.6M, the PSNR is slightly improved from 24.4 to 26.1. Note all encoders share similar architecture (Mobile-Former with 12 blocks), but have different widths.

List of interesting findings: (a) placing the compressed embedding q in the corner instead of the center introduces negligible degradation, (b) the reconstruction from the averaged \bar{q} over 50k images in the validation set is a gray image, (c) most embeddings sampled from the statistics in the validation set correspond to noise images, and (d) the straight line between the embeddings of two images $\alpha q_1 + (1 - \alpha)q_2$ corresponds to their mix-up. Please refer to Appendix E for details.

5 Self-supervised Pre-training Experiments

In this section, we evaluate masked FINOLA in self-supervised pre-training. We focus on the block-wise masked FINOLA (FINOLA-B) and assess its performance in ImageNet-1K classification and

Table 3: **Comparisons with supervised pre-training**, evaluated on ImageNet-1K. The fine-tuning performance for FINOLA pre-training is reported to compare with the supervised counterpart. Three Mobile-Former backbones with different widths (720, 1440, 2880) are used. Each is followed by a `tran-1` decoder that includes a single transformer block. Masked FINOLA consistently outperforms the supervised counterpart over three models. The gain increases as the model gets wider.

encoder	pre-training	top-1
MF-W720	supervised	75.7
	FINOLA	75.8
MF-W1440	supervised	79.4
	FINOLA	80.5
MF-W2880	supervised	80.8
	FINOLA	82.5

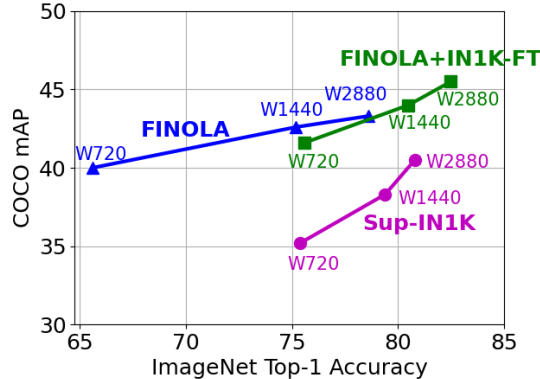


Figure 7: **Task-agnostic encoders** evaluated on ImageNet (IN-1K) classification and COCO object detection. We compare three IN-1K pretraining methods: (a) supervised (**Sup-IN1K**), (b) masked **FINOLA**, and (c) masked FINOLA with fine-tuning on IN-1K (**FINOLA+IN1K-FT**). The dots represent different Mobile-Former backbone widths. For classification, a `tran-1` decoder is added and trained with class supervision. Note that the backbone is frozen during object detection, shared by both tasks. **FINOLA** lags behind **Sup-IN1K** in classification but surpasses it in object detection. After fine-tuning on IN-1K, **FINOLA+IN1K-FT** improves for both tasks, offering robust task-agnostic encoders.

COCO object detection. For brevity, we use the term "FINOLA" to refer to Masked FINOLA-B throughout the remainder of this section. Our evaluation demonstrates two findings: (a) FINOLA provides a robust task-agnostic encoder for both tasks, without requiring COCO-specific fine-tuning, and (b) FINOLA effectively enables compact models for self-supervised learning. Please refer to Appendix B, C and F for network structure, training setup, and additional experiments respectively.

5.1 Robust Task Agnostic Encoder for ImageNet Classification and COCO Object Detection

Below, we present a comparison of FINOLA with supervised and MoCo-V2 baselines on task-agnostic encoder pre-training, specifically without COCO-specific fine-tuning (but ImageNet fine-tuning is allowed). Three Mobile-Former variants with varying widths are employed as encoders. For image classification, we utilize two decoders: a linear decoder (`lin`) and a single transformer block decoder (`tran-1`). In the case of COCO object detection, we employ a nine-layer Mobile-Former decoder (MF-Dec-522) within the DETR framework [5] (see Appendix B for network details).

Comparisons with supervised pre-training: FINOLA pre-training followed by ImageNet-1K (IN-1K) fine-tuning consistently outperforms IN-1K supervised pre-training on both ImageNet classification (see Table 3) and COCO object detection (see Table 4), providing strong task-agnostic encoders. Figure 7 visualize the comparison in one plot. The gains on object detection are significant i.e. 5–6.4 AP. Remarkably, even FINOLA pre-training alone (without IN-1K fine-tuning) outperforms the supervised counterpart on object detection by a clear margin 3–4.5 AP. This demonstrates FINOLA’s capability to encode spatial structures.

Comparisons with MoCo-v2: As shown in Table 5, FINOLA demonstrates comparable performance to MoCo-V2 in linear probing, while surpassing MoCo-V2 in `tran-1` probing, IN-1K fine-tuning, and object detection. `tran-1` probing freezes the encoder and trains a single transformer block as a decoder using class labels. FINOLA’s superior performance suggests it learns more effective intermediate features, contributing to more representative decoder features. Furthermore, the improved performance in object detection emphasizes FINOLA’s ability to encode spatial structures effectively.

These experiments demonstrate that the proposed masked FINOLA is able to learn task-agnostic representation by using a simple masking design. This supports that the underlying PDEs capture the intrinsic spatial structures present in images.

Table 4: **COCO object detection results** on the val2017 dataset using a *frozen* backbone pre-trained on ImageNet-1K. The evaluation is performed with three different Mobile-Former [14] backbones within the DETR [5] framework. Our FINOLA consistently outperform the supervised counterpart. Notably, fine-tuning on ImageNet-1K (denoted as "IN-ft") yields further improvements. The madds metric is based on an image size of 800×1333 .

head			backbone				pre-train	IN-ft	AP	AP ₅₀	AP ₇₅	AP _S	AP _M	AP _L
model	madds (G)	param (M)	model	madds (G)	param (M)									
MF	34.6	19.4	MF W2880	77.5	25.0	supervised	–	40.5	58.5	43.3	21.1	43.4	56.8	
						FINOLA	✗	43.3 ^(+2.8)	61.5	46.8	23.7	46.9	60.1	
						FINOLA	✓	45.5 ^(+5.0)	63.8	49.5	25.1	49.1	63.5	
Dec	32.3	18.6	MF W1440	20.4	11.7	supervised	–	38.3	56.0	40.8	19.0	40.9	54.3	
						FINOLA	✗	42.6 ^(+4.3)	60.3	46.1	22.6	46.2	60.0	
						FINOLA	✓	44.0 ^(+5.7)	62.3	47.3	23.8	47.6	61.0	
522	31.1	18.2	MF W720	5.6	4.9	supervised	–	35.2	52.1	37.6	16.9	37.2	51.7	
						FINOLA	✗	40.0 ^(+4.8)	57.9	42.9	20.6	43.3	56.8	
						FINOLA	✓	41.6 ^(+6.4)	59.4	45.0	21.2	45.0	58.9	

Table 5: **Comparisons with MoCo-v2** on ImageNet classification and COCO object detection. Three Mobile-Former backbones with different widths are used. In `tran-1`, the encoder is frozen while a transformer block is trained as a decoder using class labels. In `tran-1-ft`, encoders are fine-tuned. FINOLA outperforms MoCo-V2 in most evaluations, except on par in linear probing.

pre-training	encoder	ImageNet classification (top-1)			COCO object detection (AP)	
		lin	tran-1	tran-1-ft	w/o IN-ft	with IN-ft
MoCo-V2 [10]	MF-W720	51.6	52.9	74.3	31.8	39.9
FINOLA		51.3	65.5	75.6	40.0	41.6
MoCo-V2 [10]	MF-W1440	60.4	58.5	79.2	30.3	39.0
FINOLA		62.8	75.2	80.5	42.6	44.0
MoCo-V2 [10]	MF-W2880	66.5	63.8	80.0	25.5	31.7
FINOLA		66.4	78.7	82.5	43.3	45.5

5.2 Effective Self-supervised Pre-training for Efficient Models

In this subsection, we compare our method with previous approaches as complete end-to-end systems. For instance, we compare the performance of FINOLA+MobileFormer with MAE+ViT in the context of ImageNet classification. Similarly, we compare the results of FINOLA+MobileFormer+DETR with Supervised+ResNet+DN-DETR for COCO object detection. These comparisons provide insights into the effectiveness and competitiveness of our approach across different tasks.

Linear probing on ImageNet-1K: In Table 6, we compare FINOLA with previous masked prediction methods, highlighting its advantage in pre-training smaller models. Notably, FINOLA achieves a remarkable accuracy of 62.8% on a Mobile-Former model with 14 million parameters, surpassing the performance of MAE with ViT-S (22M parameters) and BEiT with ViT-B (86M parameters).

Fine-tuning on ImageNet-1K: Table 7 compares FINOLA with MAE and MoCo-V3 on fine-tuning results. Here, FINOLA uses Mobile-Former as the encoder followed by `tran-4` decoder (4 transformer blocks). Compared to the MAE pre-trained ViT, FINOLA achieves comparable performance but costs lower FLOPs.

Fine-tuning on COCO: Fine-tuning on COCO further enhances the performance of FINOLA (see Table 8). FINOLA-DETR, trained with a fine-tuned backbone in the DETR framework, achieves an AP of 49.0, outperforming most DETR-based detectors except DINO [53]. Remarkably, our method achieves these results while using significantly fewer FLOPs (112G vs. 279G) and object queries (100 vs. 900). When compared to DETR-DC5 with a fine-tuned backbone, FINOLA-DETR with a *frozen* backbone achieves a 2.2 AP improvement while reducing MAdds by 40%.

These results showcase the efficacy of FINOLA in capturing rich image representations even with more compact models, offering a promising approach for efficient self-supervised learning.

Table 6: **Comparison with masked encoding methods on ImageNet-1K using linear probing.** FINOLA pre-training demonstrates the ability to learn effective representations in a self-supervised manner for small models. † denotes our implementation.

method	model	params	top-1
iGPT [7]	iGPT-L	1362M	69.0
BEiT [2]	ViT-B	86M	56.7
SimMIM [50]	ViT-B	86M	56.7
MAE [25]	ViT-B	86M	68.0
MAE [25]†	ViT-S	22M	49.2
MAE-Lite [47]	ViT-Tiny	6M	23.3
FINOLA	MF-W720	6M	51.3
FINOLA	MF-W1440	14M	62.8
FINOLA	MF-W2880	28M	66.4

Table 7: **Comparison with previous self-supervised methods on ImageNet-1K fine-tuning.** Three Mobile-Former backbones of varying widths are used, followed by a tran-4 decoder with 4 transformer blocks. FINOLA achieves comparable performance to MAE while requiring lower computational cost.

method	model	madds	params	top-1
MoCo-v3 [13]	ViT-Tiny	1.2G	6M	76.8
MAE-Lite [47]	ViT-Tiny	1.2G	6M	78.0
FINOLA	MF-W720	0.7G	7M	78.4
MoCo-v3 [13]	ViT-S	4.6G	22M	81.4
MAE-Lite [47]	ViT-S	4.6G	22M	82.1
FINOLA	MF-W1440	2.6G	20M	82.2
MoCo-v3 [13]	ViT-B	16.8G	86M	83.2
MAE [25]	ViT-B	16.8G	86M	83.6
FINOLA	MF-W2880	9.9G	57M	83.9

Table 8: **Comparison with DETR-based models on COCO detection.** All baselines are fine-tuned on COCO. FINOLA-DETR utilizes Mobile-Former (MF-W2880) as the backbone, which has similar FLOPs and model size to the ResNet-50 used in other methods. MAdds are calculated based on an image size of 800×1333 .

model	query	AP	AP ₅₀	AP ₇₅	AP _S	AP _M	AP _L	madds (G)	param (M)
DETR-DC5[5]	100	43.3	63.1	45.9	22.5	47.3	61.1	187	41
Deform-DETR[55]	300	46.2	65.2	50.0	28.8	49.2	61.7	173	40
DAB-DETR[35]	900	46.9	66.0	50.8	30.1	50.4	62.5	195	48
DN-DETR[32]	900	48.6	67.4	52.7	31.0	52.0	63.7	195	48
DINO[53]	900	50.9	69.0	55.3	34.6	54.1	64.6	279	47
FINOLA-DETR (frozen)		45.5	63.8	49.5	25.1	49.1	63.5		
FINOLA-DETR (fine-tune)	100	49.0	67.7	53.4	30.1	52.9	65.5	112	44

6 Related Work

Autoregressive image modeling [44, 43, 40, 12, 52] uses conditional probability distributions to generate high-quality images based on previously generated pixels. These models have evolved from pixel-level focus to operating in the latent space using vector quantization [46, 39, 20]. In contrast, our method shows image is first-order, norm+linear autoregressive over a continuous space deterministically.

Masked image modeling (MIM) is inspired by the success of BERT [16] and ViT [19] to learn representation by predicting masked region from unmasked counterpart. BEiT [2] and PeCo [17] predict on tokens, MaskFeat [48] predicts on HOG, and MAE [25] reconstructs original pixels. Recent works further explore combining MIM and contrastive learning [54, 18, 28, 42, 1, 29] or techniques suitable for ConvNets [22, 30, 21]. Different from these works that use random masking, FINOLA uses regular masking and simpler norm+linear prediction.

Contrastive methods [3, 24, 45, 49, 26, 11, 6] achieve significant progress. They are most applied to Siamese architectures [8, 26, 10, 13] to contrast image similarity and dissimilarity and rely on data augmentation. [11, 23] remove dissimilarity between negative samples by handling collapse carefully. [9, 33] show pre-trained models work well for semi-supervised learning and few-shot transfer.

7 Limitations

The major limitation of our image reconstruction method is the loss of high-frequency details, as demonstrated in Figure 1. The resulting images exhibit blurred faces, trees, and deformed small texts. This limitation may be attributed to the choice of loss function, as we currently use the mean square

error. In future work, we plan to explore the use of adversarial loss, as suggested in VQGAN [20], to promote high-quality reconstruction and address this limitation.

8 Conclusion

This paper introduces FINOLA, a novel framework that represents every image as a first-order norm+linear autoregressive process. This discovery unveils the existence of underlying partial differential equations (PDEs) governing the latent feature space, shedding new light on the understanding of image representations. Furthermore, FINOLA is explored in self-supervised learning, employing a simple masked prediction technique. Remarkably, the pre-trained FINOLA representation is effective for image classification and object detection tasks, even within lightweight networks, eliminating the need for extensive fine-tuning. Overall, FINOLA offers insights into the mathematical foundations of image processing and showcasing its practical utility in various computer vision applications.

References

- [1] M. Assran, M. Caron, I. Misra, P. Bojanowski, F. Bordes, P. Vincent, A. Joulin, M. Rabbat, and N. Ballas. Masked siamese networks for label-efficient learning. *arXiv preprint arXiv:2204.07141*, 2022.
- [2] H. Bao, L. Dong, and F. Wei. BEiT: BERT pre-training of image transformers. 2021.
- [3] S. Becker and G. E. Hinton. A self-organizing neural network that discovers surfaces in random-dot stereograms. *Nature*, 355:161–163, 1992.
- [4] T. Brown, B. Mann, N. Ryder, M. Subbiah, J. D. Kaplan, P. Dhariwal, A. Neelakantan, P. Shyam, G. Sastry, A. Askell, S. Agarwal, A. Herbert-Voss, G. Krueger, T. Henighan, R. Child, A. Ramesh, D. Ziegler, J. Wu, C. Winter, C. Hesse, M. Chen, E. Sigler, M. Litwin, S. Gray, B. Chess, J. Clark, C. Berner, S. McCandlish, A. Radford, I. Sutskever, and D. Amodei. Language models are few-shot learners. In H. Larochelle, M. Ranzato, R. Hadsell, M. Balcan, and H. Lin, editors, *Advances in Neural Information Processing Systems*, volume 33, pages 1877–1901. Curran Associates, Inc., 2020.
- [5] N. Carion, F. Massa, G. Synnaeve, N. Usunier, A. Kirillov, and S. Zagoruyko. End-to-end object detection with transformers. In *ECCV*, 2020.
- [6] M. Caron, H. Touvron, I. Misra, H. Jégou, J. Mairal, P. Bojanowski, and A. Joulin. Emerging properties in self-supervised vision transformers. In *Proceedings of the International Conference on Computer Vision (ICCV)*, 2021.
- [7] M. Chen, A. Radford, R. Child, J. Wu, H. Jun, P. Dhariwal, D. Luan, and I. Sutskever. Generative pretraining from pixels. 2020.
- [8] T. Chen, S. Kornblith, M. Norouzi, and G. Hinton. A simple framework for contrastive learning of visual representations. *arXiv preprint arXiv:2002.05709*, 2020.
- [9] T. Chen, S. Kornblith, K. Swersky, M. Norouzi, and G. Hinton. Big self-supervised models are strong semi-supervised learners. *arXiv preprint arXiv:2006.10029*, 2020.
- [10] X. Chen, H. Fan, R. Girshick, and K. He. Improved baselines with momentum contrastive learning. *arXiv preprint arXiv:2003.04297*, 2020.
- [11] X. Chen and K. He. Exploring simple siamese representation learning. *arXiv preprint arXiv:2011.10566*, 2020.
- [12] X. Chen, N. Mishra, M. Rohaninejad, and P. Abbeel. PixelSNAIL: An improved autoregressive generative model. In *Proceedings of the 35th International Conference on Machine Learning*, pages 864–872, 2018.
- [13] X. Chen*, S. Xie*, and K. He. An empirical study of training self-supervised vision transformers. *arXiv preprint arXiv:2104.02057*, 2021.
- [14] Y. Chen, X. Dai, D. Chen, M. Liu, X. Dong, L. Yuan, and Z. Liu. Mobile-former: Bridging mobilenet and transformer. In *Proceedings of the IEEE/CVF Conference on Computer Vision and Pattern Recognition (CVPR)*, 2022.
- [15] J. Deng, W. Dong, R. Socher, L.-J. Li, K. Li, and L. Fei-Fei. Imagenet: A large-scale hierarchical image database. In *2009 IEEE conference on computer vision and pattern recognition*, pages 248–255. Ieee, 2009.
- [16] J. Devlin, M.-W. Chang, K. Lee, and K. Toutanova. BERT: Pre-training of deep bidirectional transformers for language understanding. In *Proceedings of the 2019 Conference of the North American Chapter of the Association for Computational Linguistics: Human Language Technologies*, pages 4171–4186, Minneapolis, Minnesota, June 2019.

- [17] X. Dong, J. Bao, T. Zhang, D. Chen, W. Zhang, L. Yuan, D. Chen, F. Wen, and N. Yu. Peco: Perceptual codebook for BERT pre-training of vision transformers. *abs/2111.12710*, 2021.
- [18] X. Dong, J. Bao, T. Zhang, D. Chen, W. Zhang, L. Yuan, D. Chen, F. Wen, and N. Yu. Bootstrapped masked autoencoders for vision bert pretraining. *arXiv preprint arXiv:2207.07116*, 2022.
- [19] A. Dosovitskiy, L. Beyer, A. Kolesnikov, D. Weissenborn, X. Zhai, T. Unterthiner, M. Dehghani, M. Minderer, G. Heigold, S. Gelly, J. Uszkoreit, and N. Houlsby. An image is worth 16x16 words: Transformers for image recognition at scale. In *International Conference on Learning Representations*, 2021.
- [20] P. Esser, R. Rombach, and B. Ommer. Taming transformers for high-resolution image synthesis. In *Proceedings of the IEEE/CVF Conference on Computer Vision and Pattern Recognition (CVPR)*, pages 12873–12883, June 2021.
- [21] Y. Fang, L. Dong, H. Bao, X. Wang, and F. Wei. Corrupted image modeling for self-supervised visual pre-training. *ArXiv*, abs/2202.03382, 2022.
- [22] P. Gao, T. Ma, H. Li, J. Dai, and Y. Qiao. Convmae: Masked convolution meets masked autoencoders. *arXiv preprint arXiv:2205.03892*, 2022.
- [23] J.-B. Grill, F. Strub, F. Altché, C. Tallec, P. H. Richemond, E. Buchatskaya, C. Doersch, B. A. Pires, Z. D. Guo, M. G. Azar, B. Piot, K. Kavukcuoglu, R. Munos, and M. Valko. Bootstrap your own latent: A new approach to self-supervised learning, 2020.
- [24] R. Hadsell, S. Chopra, and Y. LeCun. Dimensionality reduction by learning an invariant mapping. In *2006 IEEE Computer Society Conference on Computer Vision and Pattern Recognition (CVPR'06)*, volume 2, pages 1735–1742, 2006.
- [25] K. He, X. Chen, S. Xie, Y. Li, P. Dollár, and R. Girshick. Masked autoencoders are scalable vision learners. *arXiv:2111.06377*, 2021.
- [26] K. He, H. Fan, Y. Wu, S. Xie, and R. Girshick. Momentum contrast for unsupervised visual representation learning. *arXiv preprint arXiv:1911.05722*, 2019.
- [27] K. He, X. Zhang, S. Ren, and J. Sun. Deep residual learning for image recognition. In *Proceedings of the IEEE conference on computer vision and pattern recognition*, pages 770–778, 2016.
- [28] Z. Huang, X. Jin, C. Lu, Q. Hou, M.-M. Cheng, D. Fu, X. Shen, and J. Feng. Contrastive masked autoencoders are stronger vision learners. *arXiv preprint arXiv:2207.13532*, 2022.
- [29] Z. Jiang, Y. Chen, M. Liu, D. Chen, X. Dai, L. Yuan, Z. Liu, and Z. Wang. Layer grafted pre-training: Bridging contrastive learning and masked image modeling for better representations. In *International Conference on Learning Representations*.
- [30] L. Jing, J. Zhu, and Y. LeCun. Masked siamese convnets. *CoRR*, abs/2206.07700, 2022.
- [31] J. Lee, Y. Lee, J. Kim, A. Kosiorek, S. Choi, and Y. W. Teh. Set transformer: A framework for attention-based permutation-invariant neural networks. In *Proceedings of the 36th International Conference on Machine Learning*, pages 3744–3753, 2019.
- [32] F. Li, H. Zhang, S. Liu, J. Guo, L. M. Ni, and L. Zhang. Dn-detr: Accelerate detr training by introducing query denoising. In *Proceedings of the IEEE/CVF Conference on Computer Vision and Pattern Recognition*, pages 13619–13627, 2022.
- [33] S. Li, D. Chen, Y. Chen, L. Yuan, L. Zhang, Q. Chu, B. Liu, and N. Yu. Improve unsupervised pretraining for few-label transfer. In *Proceedings of the IEEE/CVF International Conference on Computer Vision (ICCV)*, pages 10201–10210, October 2021.
- [34] Y. Li, Y. Chen, X. Dai, D. Chen, M. Liu, L. Yuan, Z. Liu, L. Zhang, and N. Vasconcelos. Micronet: Improving image recognition with extremely low flops. In *International Conference on Computer Vision*, 2021.
- [35] S. Liu, F. Li, H. Zhang, X. Yang, X. Qi, H. Su, J. Zhu, and L. Zhang. DAB-DETR: Dynamic anchor boxes are better queries for DETR. In *International Conference on Learning Representations*, 2022.
- [36] A. Radford, K. Narasimhan, T. Salimans, and I. Sutskever. Improving language understanding by generative pre-training. 2018.
- [37] A. Radford, J. Wu, R. Child, D. Luan, D. Amodei, and I. Sutskever. Language models are unsupervised multitask learners. 2019.
- [38] A. Ramesh, M. Pavlov, G. Goh, S. Gray, C. Voss, A. Radford, M. Chen, and I. Sutskever. Zero-shot text-to-image generation, 2021. cite arxiv:2102.12092.
- [39] A. Razavi, A. van den Oord, and O. Vinyals. Generating diverse high-fidelity images with vq-vae-2. In *Advances in Neural Information Processing Systems*, volume 32. Curran Associates, Inc., 2019.
- [40] T. Salimans, A. Karpathy, X. Chen, and D. P. Kingma. Pixelcnn++: A pixelcnn implementation with discretized logistic mixture likelihood and other modifications. In *ICLR*, 2017.

- [41] M. Sandler, A. Howard, M. Zhu, A. Zhmoginov, and L.-C. Chen. Mobilenetv2: Inverted residuals and linear bottlenecks. In *Proceedings of the IEEE Conference on Computer Vision and Pattern Recognition*, pages 4510–4520, 2018.
- [42] C. Tao, X. Zhu, G. Huang, Y. Qiao, X. Wang, and J. Dai. Siamese image modeling for self-supervised vision representation learning, 2022.
- [43] A. van den Oord, N. Kalchbrenner, L. Espeholt, k. kavukcuoglu, O. Vinyals, and A. Graves. Conditional image generation with pixelcnn decoders. In D. Lee, M. Sugiyama, U. Luxburg, I. Guyon, and R. Garnett, editors, *Advances in Neural Information Processing Systems*, volume 29. Curran Associates, Inc., 2016.
- [44] A. van den Oord, N. Kalchbrenner, and K. Kavukcuoglu. Pixel recurrent neural networks. In *Proceedings of The 33rd International Conference on Machine Learning*, pages 1747–1756, 2016.
- [45] A. van den Oord, Y. Li, and O. Vinyals. Representation learning with contrastive predictive coding. *ArXiv*, abs/1807.03748, 2018.
- [46] A. van den Oord, O. Vinyals, and k. kavukcuoglu. Neural discrete representation learning. In I. Guyon, U. V. Luxburg, S. Bengio, H. Wallach, R. Fergus, S. Vishwanathan, and R. Garnett, editors, *Advances in Neural Information Processing Systems*, volume 30. Curran Associates, Inc., 2017.
- [47] S. Wang, J. Gao, Z. Li, J. Sun, and W. Hu. A closer look at self-supervised lightweight vision transformers. *arXiv preprint arXiv:2205.14443*, 2022.
- [48] C. Wei, H. Fan, S. Xie, C.-Y. Wu, A. Yuille, and C. Feichtenhofer. Masked feature prediction for self-supervised visual pre-training. In *Proceedings of the IEEE/CVF Conference on Computer Vision and Pattern Recognition (CVPR)*, pages 14668–14678, June 2022.
- [49] Z. Wu, Y. Xiong, X. Y. Stella, and D. Lin. Unsupervised feature learning via non-parametric instance discrimination. In *Proceedings of the IEEE Conference on Computer Vision and Pattern Recognition*, 2018.
- [50] Z. Xie, Z. Zhang, Y. Cao, Y. Lin, J. Bao, Z. Yao, Q. Dai, and H. Hu. Simsim: A simple framework for masked image modeling. In *International Conference on Computer Vision and Pattern Recognition (CVPR)*, 2022.
- [51] J. Yu, Z. Wang, V. Vasudevan, L. Yeung, M. Seyedhosseini, and Y. Wu. Coca: Contrastive captioners are image-text foundation models. *Transactions on Machine Learning Research*, 2022.
- [52] J. Yu, Y. Xu, J. Y. Koh, T. Luong, G. Baid, Z. Wang, V. Vasudevan, A. Ku, Y. Yang, B. K. Ayan, B. Hutchinson, W. Han, Z. Parekh, X. Li, H. Zhang, J. Baldrige, and Y. Wu. Scaling autoregressive models for content-rich text-to-image generation. *Transactions on Machine Learning Research*, 2022. Featured Certification.
- [53] H. Zhang, F. Li, S. Liu, L. Zhang, H. Su, J. Zhu, L. M. Ni, and H.-Y. Shum. Dino: Detr with improved denoising anchor boxes for end-to-end object detection, 2022.
- [54] J. Zhou, C. Wei, H. Wang, W. Shen, C. Xie, A. Yuille, and T. Kong. ibot: Image bert pre-training with online tokenizer. *International Conference on Learning Representations (ICLR)*, 2022.
- [55] X. Zhu, W. Su, L. Lu, B. Li, X. Wang, and J. Dai. Deformable detr: Deformable transformers for end-to-end object detection. *arXiv preprint arXiv:2010.04159*, 2020.

A Mathematical Derivation

In this section, we present (a) a proof demonstrating the correspondence between the proposed partial differential equations and a special case of the *anisotropic Laplacian*, shedding light on their underlying connection, and (b) a calculation of the Gaussian curvature for a feature surface.

FINOLA is a special case of anisotropic Laplacian. Let us firstly review that FINOLA is essentially represented by two partial differential equations (PDEs) as:

$$\frac{\partial \mathbf{z}}{\partial x} = \mathbf{A} \mathbf{z}_n, \quad \frac{\partial \mathbf{z}}{\partial y} = \mathbf{B} \mathbf{z}_n. \quad (6)$$

Below, we will show these two PDEs correspond to a special case of Laplacian under two assumptions: (a) matrices \mathbf{A} and \mathbf{B} are invertible, and (b) the feature map $\mathbf{z}(x, y)$ possesses continuous second-order partial derivatives. The second-order derivative can be expressed as:

$$\begin{aligned} \frac{\partial^2 \mathbf{z}}{\partial x^2} &= \mathbf{A} \frac{\partial \mathbf{z}_n}{\partial x} && \text{use Equation (6)} \\ &= \mathbf{A} \mathbf{B}^{-1} \mathbf{B} \frac{\partial \mathbf{z}_n}{\partial x} && \mathbf{B} \text{ is invertible, } \mathbf{B}^{-1} \mathbf{B} = \mathbf{I} \\ &= \mathbf{A} \mathbf{B}^{-1} \frac{\partial^2 \mathbf{z}}{\partial x \partial y} && \frac{\partial^2 \mathbf{z}}{\partial x \partial y} = \frac{\partial \mathbf{B} \mathbf{z}_n}{\partial x} = \mathbf{B} \frac{\partial \mathbf{z}_n}{\partial x} \\ &\stackrel{*}{=} \mathbf{A} \mathbf{B}^{-1} \frac{\partial^2 \mathbf{z}}{\partial y \partial x} && \text{Clairaut's theorem} \\ &= \mathbf{A} \mathbf{B}^{-1} \mathbf{A} \frac{\partial \mathbf{z}_n}{\partial y} && \frac{\partial^2 \mathbf{z}}{\partial y \partial x} = \frac{\partial \mathbf{A} \mathbf{z}_n}{\partial y} = \mathbf{A} \frac{\partial \mathbf{z}_n}{\partial y} \\ &= \mathbf{A} \mathbf{B}^{-1} \mathbf{A} \mathbf{B}^{-1} \mathbf{B} \frac{\partial \mathbf{z}_n}{\partial y} && \mathbf{B} \text{ is invertible, } \mathbf{B}^{-1} \mathbf{B} = \mathbf{I} \\ &= \mathbf{A} \mathbf{B}^{-1} \mathbf{A} \mathbf{B}^{-1} \frac{\partial^2 \mathbf{z}}{\partial y^2} && \text{use Equation (6) } \frac{\partial^2 \mathbf{z}}{\partial y^2} = \mathbf{B} \frac{\partial \mathbf{z}_n}{\partial y} \\ &= (\mathbf{A} \mathbf{B}^{-1})^2 \frac{\partial^2 \mathbf{z}}{\partial y^2}, \end{aligned} \quad (7)$$

where $\stackrel{*}{=}$ denotes the use of Clairaut's theorem, i.e. $\frac{\partial^2 \mathbf{z}}{\partial x \partial y} = \frac{\partial^2 \mathbf{z}}{\partial y \partial x}$ when $\mathbf{z}(x, y)$ possesses continuous second-order partial derivatives. Thus, it is a special case of anisotropic Laplacian equation as:

$$\frac{\partial^2 \mathbf{z}}{\partial x^2} - (\mathbf{A} \mathbf{B}^{-1})^2 \frac{\partial^2 \mathbf{z}}{\partial y^2} = 0. \quad (8)$$

Calculation of Gaussian curvature: To compute the Gaussian curvature, we consider the feature map per channel as a set of 16×16 surfaces $z_k(x, y)$ in 3D space, where x , y , and z_k denote the coordinates. At each position (x, y) , the Gaussian curvature for the k^{th} channel can be determined using the following equation:

$$\kappa_k(x, y) = \frac{\frac{\partial^2 z_k}{\partial x^2} \frac{\partial^2 z_k}{\partial y^2} - \left(\frac{\partial^2 z_k}{\partial x \partial y} \right)^2}{\left(1 + \left(\frac{\partial z_k}{\partial x} \right)^2 + \left(\frac{\partial z_k}{\partial y} \right)^2 \right)^2}. \quad (9)$$

Subsequently, we rank the channels based on the root mean square of the peak positive curvature (κ_+) and the peak negative curvature (κ_-) over the surface.

B Network Architectures

In this section, we provide detailed information on the network architecture components used in our study. Specifically, we describe (a) the Mobile-Former encoders, (b) the pooler to compress the feature map into a single vector, (c) the upsamplers employed in both FINOLA and Masked FINOLA, (d) the decoders designed for image classification, and (e) the decoders tailored for object detection.

Table 9: **Specification of Mobile-Former encoders.** “bneck-lite” denotes the lite bottleneck block [34]. “M-F” denotes the Mobile-Former block and “M-F \downarrow ” denotes the Mobile-Former block for downsampling.

stage	resolution	block	MF-W2880		MF-W1440		MF-W720	
			#exp	#out	#exp	#out	#exp	#out
token			6 \times 256		6 \times 256		6 \times 192	
stem	256 ²	conv 3 \times 3	–	64	–	32	–	16
1	128 ²	bneck-lite	128	64	64	32	32	16
2	64 ²	M-F \downarrow	384	112	192	56	96	28
		M-F	336	112	168	56	84	28
3	32 ²	M-F \downarrow	672	192	336	96	168	48
		M-F	576	192	288	96	144	48
		M-F	576	192	288	96	144	48
4	16 ²	M-F \downarrow	1152	352	288	96	240	80
		M-F	1408	352	704	176	320	88
		M-F	1408	352	704	176	480	88
		M-F	2112	480	1056	240	528	120
		M-F	2880	480	1440	240	720	120
		M-F	2880	480	1440	240	720	120
		conv 1 \times 1	–	2880	–	1440	–	720

Mobile-Former encoders: Mobile-Former [14] is used as the encoder in our approach. It is a CNN-based network that extends MobileNet [41] by adding 6 global tokens in parallel. To preserve spatial details, we increase the resolution of the last stage from $\frac{1}{32}$ to $\frac{1}{16}$. We evaluate three variants of Mobile-Former, which are detailed in Table 9. Each variant consists of 12 blocks and 6 global tokens, but they differ in width (720, 1440, 2880). These models serve as the encoders (or backbones) for image reconstruction, self-supervised pre-training, and evaluation in image classification and object detection tasks. For image reconstruction, we also explore two wider models, W4320 and W5760, which increase the number of channels from W2880 by 1.5 and 2 times, respectively. It’s important to note that these models were manually designed without an architectural search for optimal parameters such as width or depth.

Pooling the compressed vector q : In both FINOLA and element-wise masked FINOLA, the compressed vector q is obtained by performing attentional pooling [31, 51] on the feature map. This pooling operation involves a single multi-head attention layer with learnable queries, where the encoder output serves as both the keys and values.

Upsamplers: The architecture details of the upsamplers for FINOLA and its two Masked FINOLA variants are presented in Table 10. The vanilla FINOLA utilizes stacked upsampling and convolution blocks, while the Masked FINOLA variants employ simpler architectures to facilitate longer training. It should be noted that the vanilla FINOLA is trained for 100 epochs on ImageNet, while Masked FINOLA is trained for 1600 epochs. As mentioned in the main submission, transformer blocks (without using positional embedding) are integrated into the upsampler of Masked-FINOLA-B to enable spatial communication, while the element-wise variant (Masked-FINOLA-E) achieves this by compressing features into q and applying element-wise autoregression.

Decoders for ImageNet classification: We utilize three decoders to evaluate the pre-trained encoders in FINOLA. These decoders are as follows:

- `lin` decoder: It consists of a single linear layer and is used for linear probing.
- `tran-1` decoder: It incorporates a shallower transformer decoder with a single transformer block followed by a linear classifier and is employed for `tran-1` probing and fine-tuning.
- `tran-4` decoder: This decoder is composed of four transformer blocks followed by a linear classifier and is utilized for fine-tuning alone.

The transformer decoders are designed with different widths (192, 384, 768) to correspond with the three Mobile-Former encoders, which have widths of 720, 1440, and 2880, respectively.

Table 10: **Specification of upsampler.** “res-conv” denotes a residual block [27] composed of two convolutional layers with a 3×3 kernel size. “up-conv” performs upsampling followed by a convolutional layer with a 3×3 kernel size. “linear” is a linear layer, responsible for converting a token in a 16×16 feature map into a $16\times 16\times 3$ image patch. The transformer blocks used in Masked-FINOLA-B do *not* require positional embedding.

resolution	FINOLA			Masked-FINOLA-E			Masked-FINOLA-B		
	block	#block	#out	block	#block	#out	block	#block	#out
16^2	res-conv	1	512				transformer	6	512
32^2	up-conv	1	512						
	res-conv	1	256						
64^2	up-conv	1	256						
	res-conv	1	256						
128^2	up-conv	1	256						
	res-conv	1	128						
256^2	up-conv	1	128						
	res-conv	1	128	linear	1	3	linear	1	3
	conv 3×3	1	3						

Table 11: **Mobile-Former decoder specifications for COCO object detection:** 100 object queries with dimension 256 are used. “down-conv” includes a 3×3 depthwise convolution (stride=2) and a pointwise convolution (256 channels). “up-conv” uses bilinear interpolation, followed by a 3×3 depthwise and a pointwise convolution. “M-F⁺” replaces the *Mobile* sub-block with a transformer block, while “M-F⁻” uses the lite bottleneck [34] to replace the *Mobile* sub-block.

stage	MF-Dec-522		MF-Dec-211	
query	100×256		100×256	
$\frac{1}{32}$	down-conv M-F ⁺	×5	down-conv M-F ⁺	×2
$\frac{1}{16}$	up-conv M-F ⁻	×2	up-conv M-F ⁻	×1
$\frac{1}{8}$	up-conv M-F ⁻	×2	up-conv M-F ⁻	×1

Decoders for object detection: The decoders used in the DETR framework with Mobile-Former [14] are described in Table 11. Both decoders consist of 100 object queries with a dimension of 256. While they share a similar structure across three scales, they differ in terms of their depths. Since the backbone network ends at a resolution of $\frac{1}{16}$, the decoder incorporates a downsampling step to further reduce the resolution to $\frac{1}{32}$. This enables the decoder to efficiently process the features for object detection.

C Training Setup

In this section, we provide detailed training setups for different tasks, including:

- Image reconstruction using FINOLA on ImageNet-1K.
- Masked FINOLA pre-training on ImageNet-1K.
- Linear probing on ImageNet-1K.
- tran-1 probing on ImageNet-1K.
- Fine-tuning on ImageNet-1K.
- COCO object detection.

FINOLA pre-training: The pre-training settings for image compression and reconstruction using FINOLA are provided in Table 12. The learning rate is scaled as $lr = base_lr \times batchsize / 256$.

Table 12: **Pre-training setting for FINOLA and masked FINOLA variants.**

config	FINOLA	Masked FINOLA
optimizer	AdamW	AdamW
base learning rate	1.5e-4	1.5e-4
weight decay	0.1	0.1
batch size	128	1024
learning rate schedule	cosine decay	cosine decay
warmup epochs	10	10
training epochs	100	1600
image size	256 ²	256 ²
augmentation	RandomResizeCrop	RandomResizeCrop

Table 13: **Settings for linear probing and tran-1 probing on ImageNet-1K:** The encoders are frozen during both tasks.

config	linear probing	tran-1 probing
optimizer	SGD	AdamW
base learning rate	0.1	0.0005
weight decay	0	0.1
batch size	4096	4096
learning rate schedule	cosine decay	cosine decay
warmup epochs	10	10
training epochs	90	200
augmentation	RandomResizeCrop	RandAug (9, 0.5)
label smoothing	–	0.1
dropout	–	0.1 (MF-W720) 0.2 (MF-W1440/W2880)
random erase	–	0 (MF-W720/W1440) 0.25 (MF-W2880)

Table 14: **Setting for end-to-end fine-tuning on ImageNet-1K.**

config	value
optimizer	AdamW
base learning rate	0.0005
weight decay	0.05
layer-wise lr decay	0.90 (MF-W720/W1440) 0.85 (MF-W2880)
batch size	512
learning rate schedule	cosine decay
warmup epochs	5
training epochs	200 (MF-W720) 150 (MF-W1440) 100 (MF-W2880)
augmentation	RandAug (9, 0.5)
label smoothing	0.1
mixup	0 (MF-W720) 0.2 (MF-W1440) 0.8 (MF-W2880)
cutmix	0 (MF-W720) 0.25 (MF-W1440) 1.0 (MF-W2880)
dropout	0.2
random erase	0.25

Masked FINOLA pre-training: Similar to the vanilla FINOLA, masked FINOLA also follows the training setup described in Table 12, but with a larger batch size due to the simpler upsampler architecture that requires less memory consumption.

Linear probing: In our linear probing, we follow the approach described in [25] by incorporating an additional BatchNorm layer without affine transformation (affine=False). Detailed settings can be found in Table 13.

tran-1 probing: The settings for tran-1 decoder probing are presented in Table 13. It is important to note that the default decoder widths are 192, 384, and 768 for MF-W720, MF-W1440, and MF-W2880, respectively.

Table 15: **FINOLA vs. masked FINOLA on ImageNet [15] classification:** Compared to masked FINOLA variants, FINOLA performs poorly on both linear probing (`lin`) and probing with a single transformer block (`tran-1`) with clear margins. Even we search over the dimension of latent space, the gap is still large, i.e. more than 20%. Block-wise masked FINOLA (Masked-FINOLA-B) outperforms the element-wise variant (Masked-FINOLA-E), achieving higher accuracy. Please note that the encoders are frozen when performing linear and `tran-1` probing.

pre-training	dim of q	lin	tran-1
FINOLA	64	10.2	20.2
	128	11.5	24.0
	256	15.0	29.0
	512	20.1	34.1
	1024	23.0	39.6
	2048	23.2	41.1
	3072	17.9	46.8
Masked FINOLA-E	512	54.1	67.8
Masked FINOLA-B	–	66.4	78.7



Figure 8: **FINOLA vs. masked FINOLA on image reconstruction:** In this comparison, the encoders of the two masked FINOLA variants are frozen, and their attentional pooling and FINOLA components are fine-tuned. To ensure a fair comparison, we replace the upsamplers in the masked FINOLA variants with the same architecture as FINOLA, trained from scratch. When compared to vanilla FINOLA, the masked variants preserve color and shape information but exhibit a loss of texture details. Best viewed in color.

End-to-end fine-tuning on ImageNet-1K: The settings for the end-to-end fine-tuning of both the encoder and `tran-1` decoder are presented in Table 14. The decoder weights are initialized from the `tran-1` probing stage.

Decoder probing on COCO object detection: In this configuration, the backbone pre-trained on ImageNet-1K is frozen, and only the decoders are trained for 500 epochs on 8 GPUs with 2 images per GPU. We employ AdamW optimizer with an initial learning rate of $1e-4$. The learning rate is decreased by a factor of 10 after 400 epochs. The weight decay is $1e-4$, and the dropout rate is 0.1.

Fine-tuning on COCO object detection: In this setting, both the encoder and decoder are fine-tuned. The fine-tuning process consists of an additional 200 epochs following the decoder probing stage. The initial learning rate for both the encoder and decoder is set to $1e-5$, which decreases to $1e-6$ after 150 epochs.

D Additional Comparison between FINOLA and Masked FINOLA

Comparison of FINOLA and masked FINOLA on ImageNet classification: Table 15 presents the results of linear and `tran-1` probing applied to the vanilla FINOLA across various dimensions of the latent space. Notably, even the highest accuracy achieved by the vanilla FINOLA falls significantly behind both masked FINOLA variants (element-wise or block-wise). This stark difference highlights the remarkable power of masked prediction in learning semantic representations.

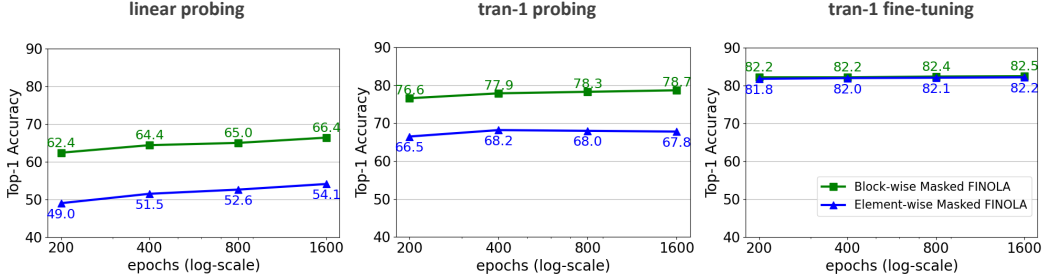


Figure 9: **Comparison of element-wise and block-wise masked FINOLA.** The evaluation includes linear probing, tran-1 probing, and tran-1 fine-tuning. Block-wise masked FINOLA consistently outperforms the element-wise counterpart across all evaluations. Notably, the performance gap in fine-tuning is smaller compared to linear and tran-1 probing. Best viewed in color.

Comparison of FINOLA and masked FINOLA on image reconstruction: Figure 8 presents a comparison of reconstructed samples obtained using FINOLA and masked FINOLA. In the case of the two masked FINOLA variants (element-wise and block-wise), the encoders are frozen, and only their attentional pooling and FINOLA components are fine-tuned. To ensure a fair comparison, we utilize the same architecture for the upsamplers in the masked FINOLA variants as in FINOLA, training them from scratch. The corresponding peak signal-to-noise ratio (PSNR) values on the ImageNet validation set are provided at the bottom. While the masked variants preserve color and shape information, they exhibit a loss of texture details compared to the vanilla FINOLA. Notably, as demonstrated in the main paper, the masked FINOLA variants demonstrate stronger semantic representation. This comparison highlights that FINOLA and masked FINOLA adhere to the same mathematical principles (involving partial differential equations) but strike different balances between semantic representation and preserving fine details.

Comparison between two Masked FINOLA variants: Figure 9 showcases the results of linear probing, tran-1 probing, and fine-tuning for two masked FINOLA variants trained with different schedules. The block-wise masked FINOLA consistently outperforms its element-wise counterpart across all evaluations. These findings demonstrate the effectiveness of directly applying FINOLA on the unmasked features to predict the masked region, as opposed to performing compression before applying FINOLA.

E Additional Experimental Results on Image Reconstruction

In this section, we present additional experimental results on image compression and reconstruction.

E.1 Main Architecture Hyper-parameters

The model size of encoder is less critical but also related. As shown in Figure 10, the larger model has better image quality. But the gap is not significant. When increasing model size by 13 times from 5.0M to 67.6M, the PSNR is slightly improved from 24.4 to 26.1. Note all encoders share similar architecture (Mobile-Former with 12 blocks), but have different widths.

The position of q is not critical: Figure 11 showcases the reconstructed samples obtained by placing the compressed vector q at different positions, including the center and four corners. The corresponding peak signal-to-noise ratio (PSNR) values on the ImageNet validation set are provided at the bottom. While placing q at the center yields slightly better results compared to corner positions, the difference is negligible. It is important to note that each positioning corresponds to its own pre-trained model with non-shared parameters.

E.2 Inspecting the Embedding Space

In this subsection, we list main observations and analysis in the space of the compressed vector q (named embedding space). This will help us to understand how images are distributed in the embedding space.

Three observations: Below we list three observations that reveal properties of the embedding space.

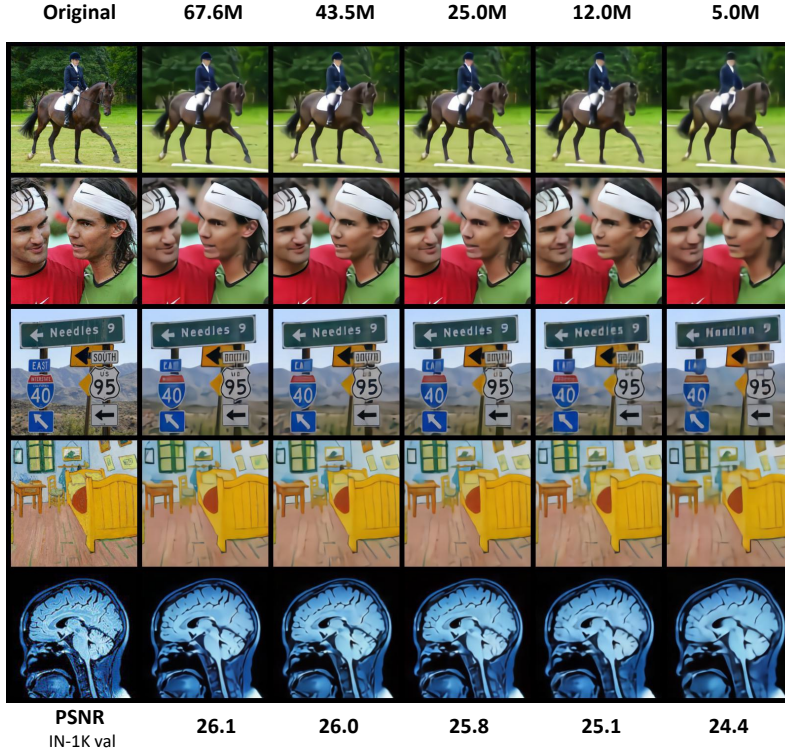


Figure 10: **Impact of encoder size on image reconstruction quality:** The image reconstruction quality shows a slight improvement as the size of the encoder increases. Even with a small encoder containing 5 million parameters (right column), it effectively compresses an image into a single vector capable of reconstructing the entire image. Best viewed in color.

Dominance of noisy images in the space: To analyze the distribution of images in the embedding space, we collected \mathbf{q} vector for all 50,000 images from the ImageNet validation set and computed their statistics (mean and covariance). By sampling embeddings based on these statistics and reconstructing images, we consistently observed the emergence of similar noisy patterns, as depicted in Figure 12. This observation highlights the prevalence of noisy images throughout the space, with good images appearing as isolated instances surrounded by the abundance of noise.

Averaged embedding $\bar{\mathbf{q}}$ yields a gray image: In Figure 13, we observe that the reconstructed image obtained from the averaged embedding $\bar{\mathbf{q}}$, computed over 50,000 images from the ImageNet validation set, closely resembles a gray image. We further investigate the relationship between real image embeddings \mathbf{q} and the averaged embedding $\bar{\mathbf{q}}$ through interpolations along the embedding space. As depicted in the *left* figure, the reconstructed images maintain their content while gradually fading into a gray image. Additionally, we extend this connection to mirror embeddings in the *right* figure, represented by $2\mathbf{q} - \bar{\mathbf{q}}$, which correspond to images with reversed colors. These findings suggest that despite the prevalence of noisy images, the line segment connecting an image embedding to the average embedding encompasses different color transformations of the same image.

Reconstruction from interpolated embeddings: In Figure 14, we present the reconstructed images obtained by interpolating between two image embeddings using the equation $\alpha\mathbf{q}_1 + (1 - \alpha)\mathbf{q}_2$. This process of embedding mixup results in a corresponding mixup of the images, allowing for a smooth transition between the two original images by varying the value of α . However, it is important to note that the resulting reconstruction may not precisely match the simple mixup of the original images, represented by $\alpha\mathbf{I}_1 + (1 - \alpha)\mathbf{I}_2$.

Combining the three observations discussed above, our findings suggest that the presence of noisy images in Figure 12 indicates the mixing of multiple surrounding images. As the number of image embeddings involved in the mixing process increases, the resulting reconstructions tend to resemble a gray image, as depicted in Figure 13.

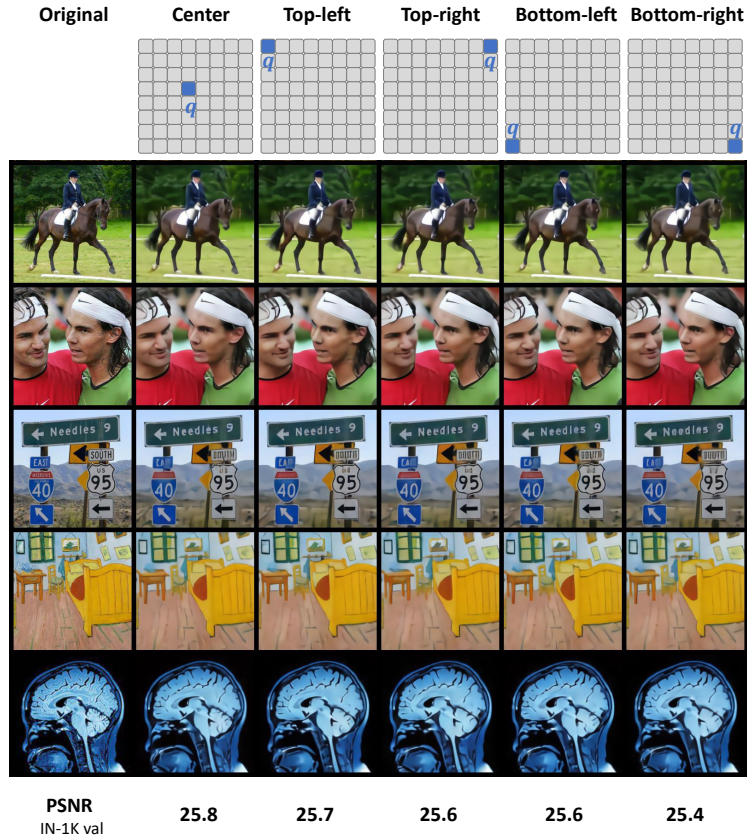


Figure 11: **Comparison of different positions of compressed vector q :** The quality of image reconstruction shows minimal sensitivity to the position of q . Placing it at the center yields slightly better results compared to corner positions. It is worth noting that each positioning has its own pre-trained model with non-shared parameters. Best viewed in color.

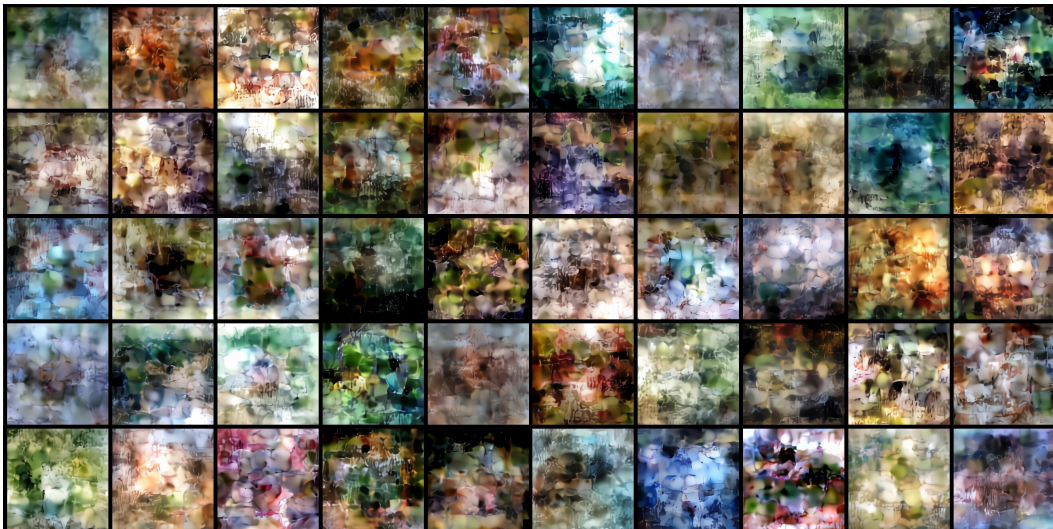


Figure 12: **Reconstruction from random samples:** The reconstructed images are generated by sampling from the statistics (mean and covariance) of compressed embeddings q obtained from the ImageNet validation set, consisting of 50,000 images. Although the samples are not similar to images of Gaussian noise, they lack semantic meaning and appear as noisy images. Multiple samplings consistently yield similar noisy patterns. Best viewed in color.



Figure 13: **Reconstruction from the average embedding \bar{q}** : The reconstructed image corresponding to the average embedding \bar{q} computed from 50,000 ImageNet validation images closely resembles a gray image (shown in the right column of the left figure). In the *left* figure, we demonstrate the interpolation along a line connecting embeddings from different images to the average embedding. Notably, the reconstructed images progressively fade into a gray image. In the *right* figure, we extend the connection between an image embedding q and the average embedding \bar{q} to a mirror embedding $2\bar{q} - q$, corresponding to an image with reversed colors. This comparison provides insights into the nature of the embedding space. Best viewed in color.

Principle component analysis (PCA): The reconstruction results shown in Figure 15 are obtained using PCA with the top- K principle components. These components correspond to the largest K eigenvalues of the covariance matrix computed from 50,000 image embeddings in the ImageNet validation set. The principle components capture essential information, starting with color and layout, and gradually encoding finer image details as more components are included in the reconstruction process.

F Additional Experiments on Self-Supervised Pre-training

In this section, we present more ablations on block-wise masked FINOLA (Masked-FINOLA-B) and additional comparisons between Masked-FINOLA-B and baselines. For brevity, we will use the term "FINOLA" to refer to Masked-FINOLA-B throughout the remainder of this section.

Ablation on training schedule: The impact of training schedule length on three Mobile-Former encoders is depicted in Figure 16. Notably, the accuracies of both linear and tran-1 probed demonstrate a consistent improvement as the training duration increases. Interestingly, even with a pre-training of just 100 epochs, fine-tuning with tran-1 achieves commendable performance. This finding diverges from the observations in MAE [25], where longer training is essential for fine-tuning improvements.

Ablation on the number of transformer blocks in the upsampler: We investigate the impact of the number of transformer blocks in the upsampler on FINOLA pre-training using the Mobile-Former-W2880 as encoder. Each transformer block in the upsampler consists of 512 channels, but does *not* use positional embedding. The results, shown in Table 16, demonstrate that adding more transformer blocks leads to consistent improvements in both linear and tran-1 probing tasks. However, we observe that the performance of fine-tuning is less sensitive to changes in the decoder depth.

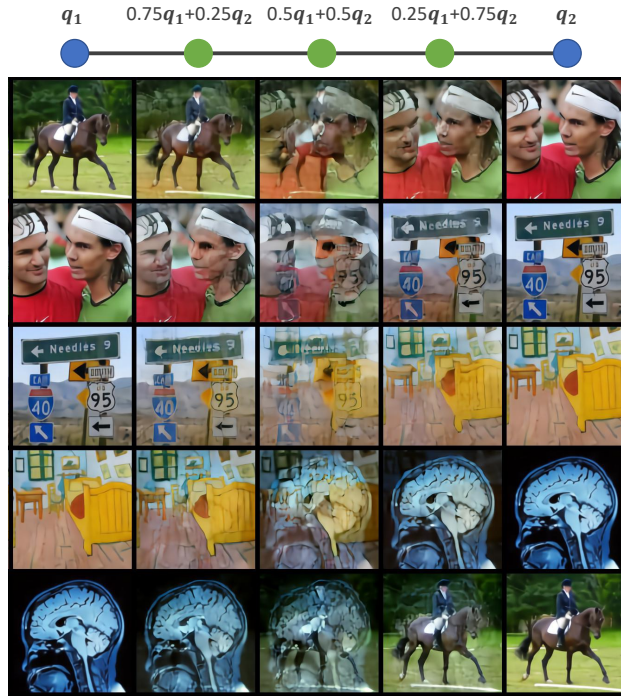


Figure 14: **Reconstruction from interpolated embeddings:** The images are reconstructed by interpolating embeddings of two images, $\alpha q_1 + (1 - \alpha)q_2$. Although the mixed embedding passes through a non-linear network that includes FINOLA and a multi-layer upsampler, it leads to mixing up images as output. Best viewed in color.



Figure 15: **Reconstruction from top principle components:** The top- K principle components correspond to the largest K eigenvalues of the covariance matrix computed from 50,000 image embeddings in the ImageNet validation set. With a selection of top-192 components (the right column), the color and layout of the images are primarily determined, but the resulting reconstructions appear blurred with noticeable loss of details. As more principle components are incorporated, the finer details are gradually restored. Best viewed in color.

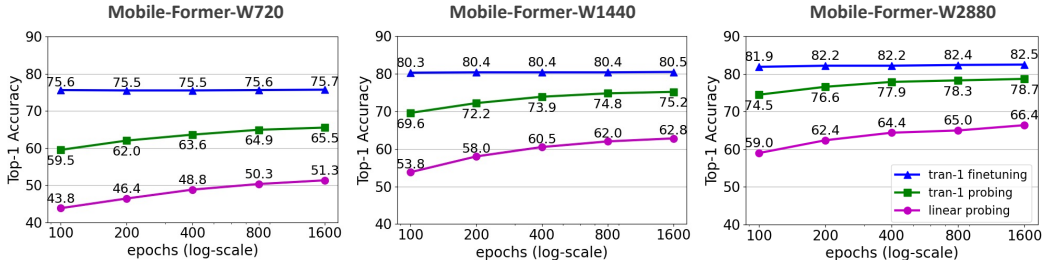


Figure 16: **Training schedules of Masked-FINOLA-B.** Longer training schedule provides consistent improvement for linear and tran-1 probing over different models, while fine-tuning performance is not sensitive to training schedule. Best viewed in color.

Table 16: **Ablation on the number of transformer blocks in the upsampler:** Evaluation is conducted on ImageNet using Mobile-Former-W2880 as the encoder. Each transformer block consists of 512 channels. Each model is pre-trained for 800 epochs. Increasing the decoder depth exhibits consistent improvement for linear and tran-1 probing, while fine-tuning performance shows limited sensitivity to decoder depth.

#blocks	lin	tran-1	tran-1-ft
1	61.1	74.4	82.2
2	62.6	76.5	82.3
3	63.5	77.3	82.2
4	63.8	78.0	82.3
5	64.0	78.1	82.3
6	65.0	78.3	82.4

Table 17: **Comparison with previous self-supervised methods on ImageNet-1K fine-tuning.** Mobile-Former-W1440 (pre-trained for 1600 epochs) is used as encoder, followed by a tran-4 decoder with 4 transformer blocks. Each transformer block consists of 384 channels. FINOLA achieves comparable performance while requiring lower computational cost.

method	model	madds	params	top-1
iBOT [54]	ViT-S	4.6G	22M	82.3
MoCo-v3 [13]	ViT-S	4.6G	22M	81.4
MAE [25]	ViT-S	4.6G	22M	79.5
MAE-Lite [47]	ViT-S	4.6G	22M	82.1
CMAE [28]	ViT-S	4.6G	22M	80.2
ConvMAE [22]	ConvViT-S	6.4G	22M	82.6
FINOLA	MF-W1440	2.6G	20M	82.2

Comparison with additional baselines on ImageNet fine-tuning: The fine-tuning results of FINOLA are compared with those of previous self-supervised methods in Table 17. For this comparison, FINOLA utilizes the Mobile-Former-W1440 encoder, followed by a tran-4 decoder consisting of four transformer blocks with 384 channels. The results demonstrate that FINOLA achieves comparable performance to the baselines while requiring lower floating-point operations (FLOPs). This highlights the effectiveness and efficiency of FINOLA in the context of self-supervised pre-training.

Comparison with the IN-1K supervised pre-training on transferring to COCO object detection: Table 18 presents the results of COCO object detection using frozen backbones. The evaluation utilizes three Mobile-Former encoders with different widths and two Mobile-Former decoders with different depths. Notably, FINOLA pre-training followed by ImageNet-1K (IN-1K) fine-tuning consistently outperforms the IN-1K supervised pre-training across all evaluations, demonstrating the effectiveness of task-agnostic encoders. Impressively, even FINOLA pre-training alone, without IN-1K fine-tuning, surpasses the supervised counterpart on object detection by a significant margin of 2.6–5.2 AP. This showcases FINOLA’s ability to encode spatial structures.

Furthermore, fine-tuning the backbone on COCO further enhances detection performance. Table 19 provides a comprehensive comparison of fine-tuning results using the Mobile-Former [14] in the DETR [5] framework. Unlike the frozen backbone configuration, where FINOLA outperforms supervised pre-training significantly (as shown in Table 18), they achieve similar performance in COCO fine-tuning. This is because the advantage of FINOLA pre-training on spatial representation diminishes when object labels in COCO provide strong guidance. However, FINOLA maintains its leading position by leveraging fine-tuning on IN-1K to improve semantic representation and transfer it to object detection. Compared to the supervised baseline, FINOLA pre-training followed by IN-1K fine-tuning achieves a gain of 0.9–2.0 AP for all three encoders and two decoders.

Table 18: **COCO object detection results** on the val2017 dataset using a *frozen* backbone pre-trained on ImageNet-1K. Evaluation is conducted over three backbones and two heads that use Mobile-Former [14] end-to-end in DETR [5] framework. Our FINOLA consistently outperform the supervised counterpart. Notably, fine-tuning on ImageNet-1K (denoted as "IN-ft") yields further improvements. The initial "MF" (e.g., MF-Dec-522) denotes Mobile-Former. The madds metric is based on an image size of 800×1333 .

model	head		backbone					AP	AP ₅₀	AP ₇₅	AP _S	AP _M	AP _L
	madds (G)	param (M)	model	madds (G)	param (M)	pre-train	IN-ft						
MF Dec 522	34.6	19.4	MF W2880	77.5	25.0	supervised	–	40.5	58.5	43.3	21.1	43.4	56.8
						FINOLA	✗	43.3 _(+2.8)	61.5	46.8	23.7	46.9	60.1
						FINOLA	✓	45.5 _(+5.0)	63.8	49.5	25.1	49.1	63.5
	32.3	18.6	MF W1440	20.4	11.7	supervised	–	38.3	56.0	40.8	19.0	40.9	54.3
						FINOLA	✗	42.6 _(+4.3)	60.3	46.1	22.6	46.2	60.0
						FINOLA	✓	44.0 _(+5.7)	62.3	47.3	23.8	47.6	61.0
	31.1	18.2	MF W720	5.6	4.9	supervised	–	35.2	52.1	37.6	16.9	37.2	51.7
						FINOLA	✗	40.0 _(+4.8)	57.9	42.9	20.6	43.3	56.8
						FINOLA	✓	41.6 _(+6.4)	59.4	45.0	21.2	45.0	58.9
MF Dec 211	15.7	9.2	MF W2880	77.5	25.0	supervised	–	34.1	51.3	36.1	15.5	36.8	50.0
						FINOLA	✗	36.7 _(+2.6)	53.7	39.3	18.2	39.7	52.2
						FINOLA	✓	41.0 _(+6.9)	59.2	44.4	20.9	44.6	58.3
	13.4	8.4	MF W1440	20.4	11.7	supervised	–	31.2	47.8	32.8	13.7	32.9	46.9
						FINOLA	✗	36.0 _(+4.8)	52.7	38.7	16.6	39.1	52.5
						FINOLA	✓	39.2 _(+8.0)	56.9	42.0	19.7	42.8	56.2
	12.2	8.0	MF W720	5.6	4.9	supervised	–	27.8	43.4	28.9	11.3	29.1	41.6
						FINOLA	✗	33.0 _(+5.2)	49.3	35.0	15.3	35.1	48.9
						FINOLA	✓	35.8 _(+8.0)	52.6	38.3	16.4	38.3	52.0

Table 19: **COCO object detection results** on the val2017 dataset after *fine-tuning* both the backbone and head on COCO. Evaluation is performed on three different backbones and two heads, utilizing the Mobile-Former [14] end-to-end in the DETR [5] framework. Our approach, which involves FINOLA pre-training followed by ImageNet-1K fine-tuning, surpasses the performance of the supervised baselines. The initial "MF" (e.g., MF-Dec-522) denotes Mobile-Former, while "IN-ft" indicates fine-tuning on ImageNet-1K. The reported madds values are based on the image size of 800×1333 .

model	head		backbone					AP	AP ₅₀	AP ₇₅	AP _S	AP _M	AP _L
	madds (G)	param (M)	model	madds (G)	param (M)	pre-train	IN-ft						
MF Dec 522	34.6	19.4	MF W2880	77.5	25.0	supervised	–	48.1	66.6	52.5	29.7	51.8	64.0
						FINOLA	✗	48.0 _(-0.1)	66.2	52.3	28.2	51.4	64.1
						FINOLA	✓	49.0 _(+0.9)	67.7	53.4	30.1	52.9	65.5
	32.3	18.6	MF W1440	20.4	11.7	supervised	–	46.2	64.4	50.1	27.1	49.8	62.4
						FINOLA	✗	46.8 _(+0.6)	64.9	51.0	26.6	50.6	63.4
						FINOLA	✓	47.3 _(+1.1)	65.6	51.4	27.3	50.7	63.9
	31.1	18.2	MF W720	5.6	4.9	supervised	–	42.5	60.4	46.0	23.9	46.0	58.5
						FINOLA	✗	43.3 _(+0.8)	61.0	47.0	23.1	46.6	61.0
						FINOLA	✓	44.4 _(+1.9)	62.1	48.1	24.3	47.8	61.5
MF Dec 211	15.7	9.2	MF W2880	77.5	25.0	supervised	–	44.0	62.8	47.7	25.8	47.3	60.7
						FINOLA	✗	44.4 _(+0.4)	62.5	48.2	24.7	47.6	60.7
						FINOLA	✓	46.0 _(+2.0)	64.8	49.9	26.2	50.0	62.7
	13.4	8.4	MF W1440	20.4	11.7	supervised	–	42.5	60.6	46.0	23.6	45.9	57.9
						FINOLA	✗	42.4 _(-0.1)	60.2	45.9	21.9	45.7	60.0
						FINOLA	✓	43.8 _(+1.3)	61.8	47.5	23.9	47.1	60.8
	12.2	8.0	MF W720	5.6	4.9	supervised	–	37.6	55.1	40.4	18.9	40.6	53.8
						FINOLA	✗	37.2 _(-0.4)	54.3	39.7	18.7	39.8	53.4
						FINOLA	✓	39.3 _(+1.7)	56.7	42.4	19.4	42.1	56.5